



In-situ X-ray diffraction study on the structural evolutions of $\text{LiNi}_{0.5}\text{Co}_{0.3}\text{Mn}_{0.2}\text{O}_2$ in different working potential windows

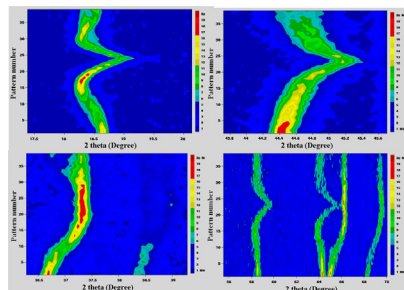
Jie Shu*, Rui Ma, Lianyi Shao, Miao Shui, Kaiqiang Wu, Mengmeng Lao, Dongjie Wang, Nengbing Long, Yuanlong Ren

Faculty of Materials Science and Chemical Engineering, Ningbo University, Ningbo 315211, Zhejiang Province, People's Republic of China

HIGHLIGHTS

- Spherical $\text{LiNi}_{0.5}\text{Co}_{0.3}\text{Mn}_{0.2}\text{O}_2$ is prepared by a co-precipitation method.
- The structural transitions from H1 to H2, H3 can be observed in 2.0–4.9 V.
- By suppressing H3, spherical LNCMO shows outstanding electrochemical properties.

GRAPHICAL ABSTRACT



ARTICLE INFO

Article history:

Received 24 April 2013

Received in revised form

8 June 2013

Accepted 9 June 2013

Available online 28 June 2013

Keywords:

Ternary layered material

Cathode

Lithium-ion batteries

In-situ X-ray diffraction technique

ABSTRACT

Spherical $\text{LiNi}_{0.5}\text{Co}_{0.3}\text{Mn}_{0.2}\text{O}_2$ samples with the particle size distribution between 10 and 20 μm are prepared by a hydroxide co-precipitation method and subsequent high temperature solid state calcination. Electrochemical results show that the reversible lithium storage capacities of spherical $\text{LiNi}_{0.5}\text{Co}_{0.3}\text{Mn}_{0.2}\text{O}_2$ cathode after 20 cycles are 121.5, 154.2 and 99.3 mAh g^{-1} in 2.0–4.3 V, 2.0–4.6 V and 2.0–4.9 V, respectively. The structural evolutions of layered materials in different working potential ranges are carefully studied by homemade *in-situ* X-ray diffraction techniques. It is found that the formation of hexagonal phase H3 is the main source resulting in poor electrochemical properties, where the hexagonal phase H2 to hexagonal phase H3 transition occurs at about 4.7 V in the charge process. As a result, it is expected that the suppression of hexagonal phase H3 can achieve a long-term cyclability and high reversible capacity for $\text{LiNi}_{0.5}\text{Co}_{0.3}\text{Mn}_{0.2}\text{O}_2$. Therefore, spherical $\text{LiNi}_{0.5}\text{Co}_{0.3}\text{Mn}_{0.2}\text{O}_2$ cathode shows the highest reversible lithium storage capacity of 154.2 mAh g^{-1} in 2.0–4.6 V after 20 cycles among all the three electrochemical working windows.

© 2013 Elsevier B.V. All rights reserved.

1. Introduction

Owing to the largest energy density and the highest output working potential of all known rechargeable batteries, lithium-ion batteries have played a key role in the rapid development of various portable electronics, such as mobile phones, laptops and electric

tools. However, the presently commercial cathodes (LiCoO_2) with practical capacity of 130–140 mAh g^{-1} in lithium-ion batteries can not meet the increasing demand for rapidly miniaturizing electronics and electric vehicles. By partial replacement of Co^{3+} with Ni^{2+} and Mn^{4+} in the structure, a high theoretical capacity of 270–280 mAh g^{-1} can be delivered for $\text{LiCo}_{1-x-y}\text{Ni}_x\text{Mn}_y\text{O}_2$ according to the reversible redox couples of $\text{Ni}^{2+/3+/4+}$ and $\text{Co}^{3+/4+}$, and an outstanding structural stability can be maintained during repeated cycles with Mn^{4+} as support in the three-dimensional framework. As a result, Ni–Co–Mn ternary transition metal cathode materials,

* Corresponding author. Tel.: +86 574 87600787; fax: +86 574 87609987.

E-mail addresses: sergio_shu@hotmail.com, shujie@nbu.edu.cn (J. Shu).



$\text{LiNi}_x\text{Co}_y\text{Mn}_z\text{O}_2$ ($x + y + z = 1$), have been developed as promising candidates for high performance lithium-ion batteries in recent years owing to higher reversible capacity and improved structural/thermal stability compared with the commercial LiCoO_2 [1–4].

As reported, Ni-deficient $\text{LiNi}_x\text{Co}_y\text{Mn}_z\text{O}_2$ ($x \leq 0.2$), such as $\text{LiNi}_{0.05}\text{Co}_{0.9}\text{Mn}_{0.05}\text{O}_2$ [5,6], can deliver a high reversible capacity ($\sim 170 \text{ mAh g}^{-1}$) over the conventional LiCoO_2 and retains over 80% of its initial capacity after hundreds of cycles. However, it suffered from expensive price, environmental pollution and structural instability, especially for poor safety. Despite decades of efforts and intense recent interests, high-capacity Ni-deficient $\text{LiNi}_x\text{Co}_y\text{Mn}_z\text{O}_2$ still show high reactivity with non-aqueous electrolytes because of the oxygen release from the highly delithiated compound, which oxidizes the electrolyte, causes flame and severe safety problems and finally leads to a severe thermal runaway. This inhibits the large-scale production of Ni-deficient $\text{LiNi}_x\text{Co}_y\text{Mn}_z\text{O}_2$ in commercial lithium-ion batteries. Thus, a series of Ni-rich $\text{LiNi}_x\text{Co}_y\text{Mn}_z\text{O}_2$ ($x \geq 0.4$) compounds are introduced for their many advantages over other candidates, namely, low cost, high capacity, superior thermal stability, and excellent cyclability [7–14]. In the previous studies, it is found that high concentration Ni^{4+} is unstable in the delithiated Ni-rich $\text{LiNi}_x\text{Co}_y\text{Mn}_z\text{O}_2$ ($x \geq 0.7$) compound and is easily reduced to Ni^{2+} to form an insulating NiO phase on the surface of cathode material, resulting in high interfacial impedance, low lithium ion diffusion coefficient and poor electrochemical properties [4,11–13]. Herein, Ni-moderate $\text{LiNi}_x\text{Co}_y\text{Mn}_z\text{O}_2$, such as $\text{LiNi}_{0.5}\text{Co}_{0.2}\text{Mn}_{0.3}\text{O}_2$ [15,16], $\text{LiNi}_{0.33}\text{Co}_{0.33}\text{Mn}_{0.33}\text{O}_2$ [1,2,17,18], and $\text{LiNi}_{0.4}\text{Co}_{0.2}\text{Mn}_{0.4}\text{O}_2$ [9,19], are always selected as host lithium-storage materials in the purpose of obtaining high capacity, good structural stability and relatively high safety cathode materials for lithium-ion batteries.

$\text{LiNi}_{0.5}\text{Co}_{0.3}\text{Mn}_{0.2}\text{O}_2$ is another member of the Ni-moderate layered materials $\text{LiNi}_x\text{Co}_y\text{Mn}_z\text{O}_2$ ($0.3 \leq x \leq 0.6$). It can be described by the R-3m space group and shows a typical $\alpha\text{-NaFeO}_2$ structure that is known of layered LiNiO_2 and LiCoO_2 . However, few published papers report the preparation and electrochemical performance of $\text{LiNi}_{0.5}\text{Co}_{0.3}\text{Mn}_{0.2}\text{O}_2$ as cathode material for lithium-ion batteries. Furthermore, the detailed working mechanisms of $\text{LiNi}_{0.5}\text{Co}_{0.3}\text{Mn}_{0.2}\text{O}_2$, especially for the evolution of $\text{Ni}^{2+}/\text{Ni}^{3+}/\text{Ni}^{4+}$, during the charge–discharge process are not well understood. Therefore, it is necessary to investigate the lithium storage behaviors of $\text{LiNi}_{0.5}\text{Co}_{0.3}\text{Mn}_{0.2}\text{O}_2$ to be a high capacity and high safety cathode material for lithium-ion batteries.

In the present study, spherical $\text{LiNi}_{0.5}\text{Co}_{0.3}\text{Mn}_{0.2}\text{O}_2$ cathode materials are prepared via a hydroxide co-precipitation method. The electrochemical behaviors are studied by using homemade simulated batteries. The structure and phase evolutions of this compound during charge–discharge process are investigated and compared in different working potential windows.

2. Experimental

2.1. Material preparation

In the experiment, all the chemical reagents were analytical grade without further purification. Spherical $\text{LiNi}_{0.5}\text{Co}_{0.3}\text{Mn}_{0.2}\text{O}_2$ samples were prepared by a hydroxide co-precipitation method. The precursor $\text{Ni}_{0.5}\text{Co}_{0.3}\text{Mn}_{0.2}[\text{OH}]_2$ coprecipitated hydroxides were synthesized by adding the LiOH solution into an aqueous mixed solution containing the required amounts (molar ratio of $\text{Ni:Co:Mn} = 5:3:2$) of Co^{2+} (from $\text{CoSO}_4 \cdot 7\text{H}_2\text{O}$), Ni^{2+} (from $\text{NiSO}_4 \cdot 6\text{H}_2\text{O}$), and Mn^{2+} (from $\text{MnSO}_4 \cdot \text{H}_2\text{O}$) under continuous stirring in a nitrogen atmosphere, and followed by filtering and washing the precipitates with distilled water. During the co-precipitation process, the concentration, pH, and temperature of the solution in the reactor were carefully controlled and adjusted.

The precipitates were dried in a vacuum oven at 80°C for 24 h and then mixed with $\text{LiOH} \cdot \text{H}_2\text{O}$ by a ball-milling method. Spherical $\text{LiNi}_{0.5}\text{Co}_{0.3}\text{Mn}_{0.2}\text{O}_2$ samples were obtained by calcining the mixture of $\text{Ni}_{0.5}\text{Co}_{0.3}\text{Mn}_{0.2}[\text{OH}]_2$ precipitates and $\text{LiOH} \cdot \text{H}_2\text{O}$ initially at 500°C for 5 h and then at 850°C for 24 h in air.

2.2. Material characterization

The crystal structure and crystalline phase of the layered samples were characterized by powder X-ray diffraction (XRD) instrument using the Bruker D8 Focus X-ray analytical systems with $\text{Cu K}\alpha$ radiation ($\lambda = 1.5406 \text{ \AA}$). The characteristic XRD patterns were refined by using Fullprof software. Fourier transform infrared (FTIR) spectra were obtained on a Shimadzu FTIR-8900 spectrometer using KBr pellet technique in the wavenumber range between 400 and 2000 cm^{-1} . Raman spectra of $\text{LiNi}_{0.5}\text{Co}_{0.3}\text{Mn}_{0.2}\text{O}_2$ were taken on a Renishaw R-1000 Raman spectrophotometer with 514.5 nm argon laser in the wavenumber range from 400 to 2000 cm^{-1} . The surface morphologies of the products were observed by means of Philips XL30 scanning electron microscopy (SEM).

2.3. Electrode preparation

The electrochemical electrodes were prepared by mixing spherical $\text{LiNi}_{0.5}\text{Co}_{0.3}\text{Mn}_{0.2}\text{O}_2$ active material, carbon black conductive additive and polyvinylidene fluoride binder with the weight ratio of 8:1:1 in N-methyl-pyrrolidone to form a homogeneous slurry. The resulting slurry was coated on an aluminum foil, and dried at 120°C for 12 h under vacuum condition, and then pressed under 50 MPa. The working electrodes were punched into discs with a diameter of 15 mm. The active material on each disc working electrode showed an average loading of 3 mg and the thickness of the active film was about $25 \mu\text{m}$. All the working electrodes were stored in the Ar-filled Etelux glove box before use.

2.4. Electrochemical characterization

The electrochemical properties of the as-prepared active materials were characterized by using homemade lithium half batteries. The symmetric simulated batteries were assembled with $\text{LiNi}_{0.5}\text{Co}_{0.3}\text{Mn}_{0.2}\text{O}_2$ film as cathode, lithium metal foil as anode, Whatman glass fiber as separator, a solution of $1 \text{ mol L}^{-1} \text{ LiPF}_6$ in ethylene carbonate and dimethyl carbonate (1:1, v/v) as electrolyte. All the testing batteries were assembled in an Etelux glove box filled with high purified argon atmosphere (moisture and oxygen contents lower than 1 ppm). Cyclic voltammograms (CVs) and galvanostatic charge–discharge cycles were performed by using computer-controlled CHI 660D electrochemical workstation at a scan rate of 0.1 mV s^{-1} and Land CT2001A multiple battery test system at a current density of 10 mA g^{-1} cycled between the limitations of 2.0 and 4.3–4.9 V, respectively. All the lithium half batteries were aged for 12 h before electrochemical measurements and all the electrochemical properties were carried out at a constant temperature (25°C).

3. Results and discussion

Fig. 1 shows the powder XRD pattern of the as-prepared $\text{LiNi}_{0.5}\text{Co}_{0.3}\text{Mn}_{0.2}\text{O}_2$ samples, where all the diffraction peaks of samples are sharp and well-defined. High temperature solid state reaction results in highly crystalline single-phase powders. All the diffraction peaks are indexed based on a hexagonal layered structure similar to LiCoO_2 and LiNiO_2 with the space group of R-3m. No evidence of impurity can be observed from the XRD pattern. The diffraction peaks at 18.64, 36.84, 37.95, 38.49, 44.50, 48.68, 58.70,

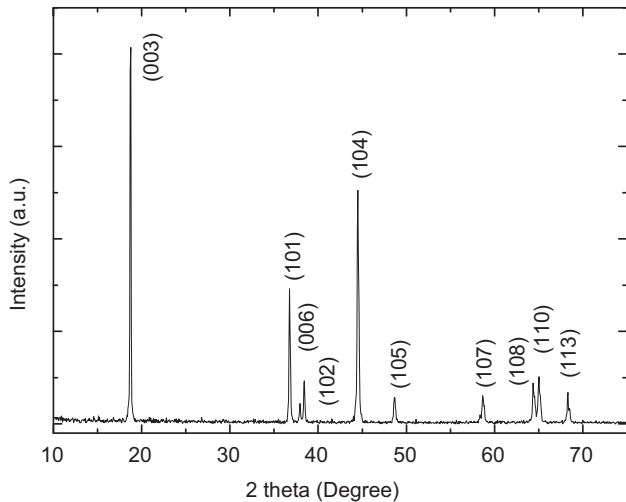


Fig. 1. XRD pattern of $\text{LiNi}_{0.5}\text{Co}_{0.3}\text{Mn}_{0.2}\text{O}_2$ prepared by a co-precipitation technique.

64.35, 65.09 and 68.37° are corresponding to the characteristic (003), (101), (006), (102), (104), (105), (107), (108), (110) and (113) lines for as-prepared $\text{LiNi}_{0.5}\text{Co}_{0.3}\text{Mn}_{0.2}\text{O}_2$ with the $\alpha\text{-NaFeO}_2$ structure, in which the transition metal ions ($\text{Ni}^{2+/\text{3}+}$, Co^{3+} and Mn^{4+}) are surrounded by six oxygen atoms to form edge-sharing $(\text{Ni},\text{Co},\text{Mn})\text{O}_6$ octahedras with Li^+ located between $(\text{Ni},\text{Co},\text{Mn})\text{O}_2$ layers. As shown in Fig. 1, the existence of doublets at (006)/(102) and (108)/(110) reflections in the XRD pattern clearly indicates the well-defined layered structure of as-prepared sample. The lattice parameters of spherical $\text{LiNi}_{0.5}\text{Co}_{0.3}\text{Mn}_{0.2}\text{O}_2$ are $a = 2.8933 \text{ \AA}$ and $c = 14.2966 \text{ \AA}$ with $c/a = 4.9413$.

The FTIR and Raman spectra of as-prepared $\text{LiNi}_{0.5}\text{Co}_{0.3}\text{Mn}_{0.2}\text{O}_2$ are shown in Fig. 2a and b. FTIR and Raman spectroscopy investigations can provide additional information on the structure of the as-obtained spherical $\text{LiNi}_{0.5}\text{Co}_{0.3}\text{Mn}_{0.2}\text{O}_2$ sample. It is well-known that the frequency and the relative intensity of the vibrational bands for FTIR and Raman spectra are strongly sensitive to the short-range local environment of oxygen coordination around the cations in the oxide lattices, involving the atomic motion of cations against their oxygen neighbors, crystal coordination symmetry and the valence states of cations. The purpose of spectroscopy study is to investigate the local environments of the transition metal cations ($\text{Ni}^{2+/\text{3}+}$, Co^{3+} and Mn^{4+}) in a cubic close-packed oxygen array of the host $\text{LiNi}_{0.5}\text{Co}_{0.3}\text{Mn}_{0.2}\text{O}_2$ lattice constituted by the alternating layers of trigonally distorted LiO_6 and $(\text{Ni},\text{Co},\text{Mn})\text{O}_6$ octahedras sharing edges. As well-known, the layered $\text{LiNi}_{0.5}\text{Co}_{0.3}\text{Mn}_{0.2}\text{O}_2$ has the spectroscopic space group of D_{3d}^5 , in which the optical vibrational modes can be described by the following equation:

$$\Gamma = 2A_{2u} + 2E_u + A_{1g} + E_g$$

The theoretical factor group analysis shows four infrared active modes ($2A_{2u}$, $2E_u$) and two Raman active modes (A_{1g} , E_g) for $\text{LiNi}_{0.5}\text{Co}_{0.3}\text{Mn}_{0.2}\text{O}_2$. However, only two infrared bands can be observed in Fig. 2a. The strong characteristic infrared bands at $500\text{--}600 \text{ cm}^{-1}$ are attributed to the vibration of M–O bonds in the structure. The FTIR absorption spectra display two features, which can be divided into two parts, the symmetrical bending of O–M–O bond (A_{2u}) centered at 530 cm^{-1} and the symmetrical stretching of M–O bond (E_u) located at 586 cm^{-1} [20,21]. No band between 400 and 500 cm^{-1} assigned to the asymmetric stretching of Li–O in LiO_6 octahedral units can be detected in Fig. 2a. The Raman characteristic bands located at 468 and 567 cm^{-1} match well with the Raman

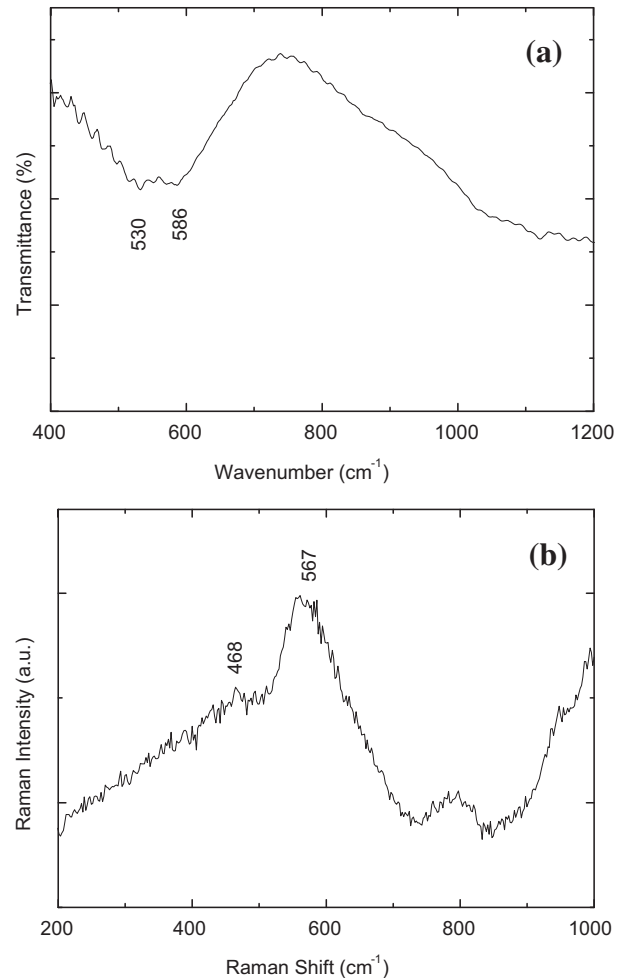


Fig. 2. FTIR and Raman spectra of $\text{LiNi}_{0.5}\text{Co}_{0.3}\text{Mn}_{0.2}\text{O}_2$.

active E_g and A_{1g} modes for the rhombohedral layered $\text{LiNi}_{0.5}\text{Co}_{0.3}\text{Mn}_{0.2}\text{O}_2$, respectively [21,22]. The Raman A_{1g} and E_g modes originate from the motion of oxygen atoms within the M–O symmetrical stretching and O–M–O bending vibrations in the hexagonal lattice of $(\text{Ni},\text{Co},\text{Mn})\text{O}_2$ layers, respectively.

The surface morphology of as-prepared $\text{LiNi}_{0.5}\text{Co}_{0.3}\text{Mn}_{0.2}\text{O}_2$ sample is displayed in Fig. 3. The SEM images of the coprecipitated products show that the as-prepared powders are composed of many uniform and spherical crystalline grains with the particle size between 10 and $20 \mu\text{m}$. The uniform Gaussian distribution of spherical particle size will result in a high tap density of $\text{LiNi}_{0.5}\text{Co}_{0.3}\text{Mn}_{0.2}\text{O}_2$ sample, which is beneficial to improve the volumetric energy and advanced applications in large-scale energy supplies. At high magnification, the SEM images of the surface of the sample reveal that the as-prepared powders are secondary particles agglomerated from highly packed primary particles with an average particle size of 500 nm . The multilayer structure of this secondary particles is favorable for the permeability of the organic electrolyte into the inner structure, and shortens the diffusion pathways of lithium ions during repeated charge–discharge cycles. As a result, the electrochemical properties of spherical $\text{LiNi}_{0.5}\text{Co}_{0.3}\text{Mn}_{0.2}\text{O}_2$ can be improved due to the hierarchical architecture.

Fig. 4 shows the CV curves of spherical $\text{LiNi}_{0.5}\text{Co}_{0.3}\text{Mn}_{0.2}\text{O}_2$ between 2.0 and 4.9 V with a scan rate of 0.1 mV s^{-1} . It can be found that there are two oxidation peaks centered at 4.12 and 4.38 V , and four reduction peaks located at 3.08 , 3.69 , 4.26 and 4.48 V appeared

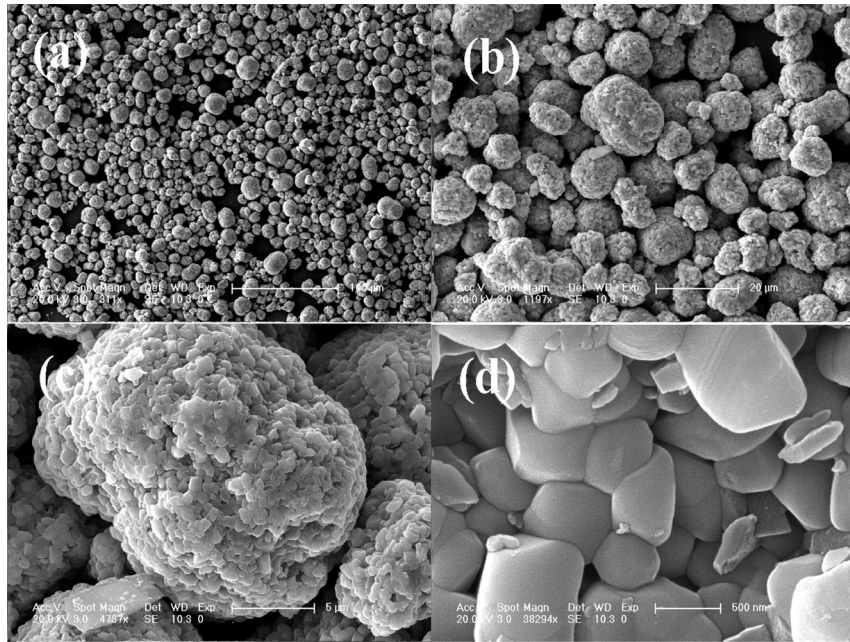


Fig. 3. SEM images of $\text{LiNi}_{0.5}\text{Co}_{0.3}\text{Mn}_{0.2}\text{O}_2$.

in the initial CV curves. The first oxidation peak (4.12 V) is predominantly contributed to the oxidation conversion from Ni^{2+} to Ni^{4+} along with the lithium ion extraction of octahedral and tetrahedral sites in the rhombohedral structure, and the second irreversible oxidation peak (4.38 V) is mainly attributed to the irreversible removal of Li_2O from the structure of $\text{LiNi}_{0.5}\text{Co}_{0.3}\text{Mn}_{0.2}\text{O}_2$ [23]. The oxidations of Ni^{3+} to Ni^{4+} and Co^{3+} to Co^{4+} also occur during the electrochemical delithiation process as the oxidation peak located at 4.22 V appeared in the second anodic scan. The subsequent reduction peaks are associated with the lithium ion occupations of octahedral (3.08 and 3.69 V) and tetrahedral (4.26 and 4.48 V) sites in the rhombohedral layered $\text{LiNi}_{0.5}\text{Co}_{0.3}\text{Mn}_{0.2}\text{O}_2$ [23–25]. Therefore, the whole Li insertion/extraction process is thermodynamically formulated as follows:

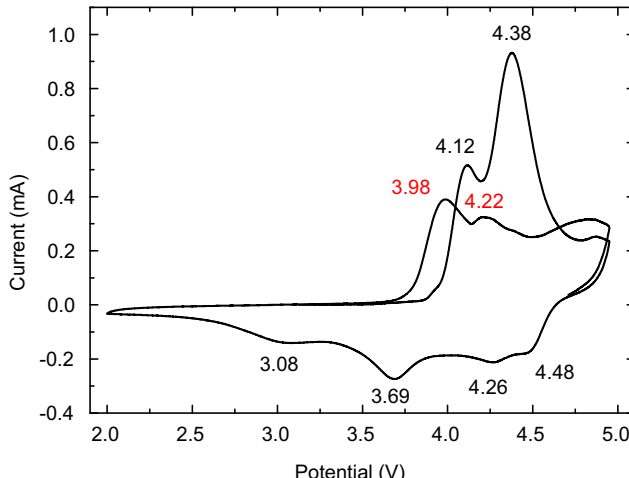
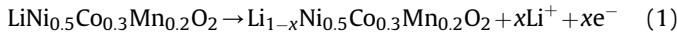
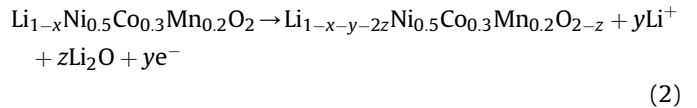


Fig. 4. CV curves of $\text{LiNi}_{0.5}\text{Co}_{0.3}\text{Mn}_{0.2}\text{O}_2$ between 2.0 and 4.9 V.



Here, x , y and z values depend on the charged/discharged states of $\text{LiNi}_{0.5}\text{Co}_{0.3}\text{Mn}_{0.2}\text{O}_2$ in different potential ranges. Besides, the oxidation formation of solid electrolyte interphase (SEI) film from electrolyte and the corresponding reduction decomposition of partial organic components from the surface film may accompany with the lithium ion insertion and extraction process for the active material working in a high potential region.

The initial five charge–discharge curves of spherical $\text{LiNi}_{0.5}\text{Co}_{0.3}\text{Mn}_{0.2}\text{O}_2$ in different electrochemical working windows are shown in Fig. 5. The first charge capacity and discharge capacity of spherical $\text{LiNi}_{0.5}\text{Co}_{0.3}\text{Mn}_{0.2}\text{O}_2$ cathode cycled between 2.0 and 4.3 V are 167.3 and 135.4 mAh g^{-1} , respectively. The initial coulombic efficiency is 80.9% as shown in Fig. 5a. Increasing the upper cutoff limitation to 4.6 V, the first charge capacity and discharge capacity of spherical $\text{LiNi}_{0.5}\text{Co}_{0.3}\text{Mn}_{0.2}\text{O}_2$ are 261.4 and 181.1 mAh g^{-1} , respectively. The corresponding initial coulombic efficiency is 69.3%. Making the upper cutoff limitation to 4.9 V, the initial charge capacity and discharge capacity of spherical $\text{LiNi}_{0.5}\text{Co}_{0.3}\text{Mn}_{0.2}\text{O}_2$ are 294.1 and 202.2 mAh g^{-1} , respectively. The corresponding initial coulombic efficiency is 68.7%. All these evidences show that spherical $\text{LiNi}_{0.5}\text{Co}_{0.3}\text{Mn}_{0.2}\text{O}_2$ cycled in higher potential region exhibits higher lithium extraction capacity but lower coulombic efficiency.

Fig. 6 shows the 1st, 10th and 20th dQ/dV curves originated from corresponding charge–discharge curves and their electrochemical cycling properties in different electrochemical working windows. As seen from Fig. 6a–c, the dQ/dV peak almost retains the original shape and peak value in the potential range from 2.0 to 4.3–4.6 V, but decreases evidently when the sample is cycled between 2.0 and 4.9 V. Capacity vs cycle number plots of spherical $\text{LiNi}_{0.5}\text{Co}_{0.3}\text{Mn}_{0.2}\text{O}_2$ in different working windows are compared in Fig. 6d. The data demonstrate that the evolution of dQ/dV peaks during repeated electrochemical cycles. It can be found that the reversible discharge capacities of spherical $\text{LiNi}_{0.5}\text{Co}_{0.3}\text{Mn}_{0.2}\text{O}_2$ after 20 cycles are 121.5, 154.2 and 99.3 mAh g^{-1} in 2.0–4.3 V, 2.0–

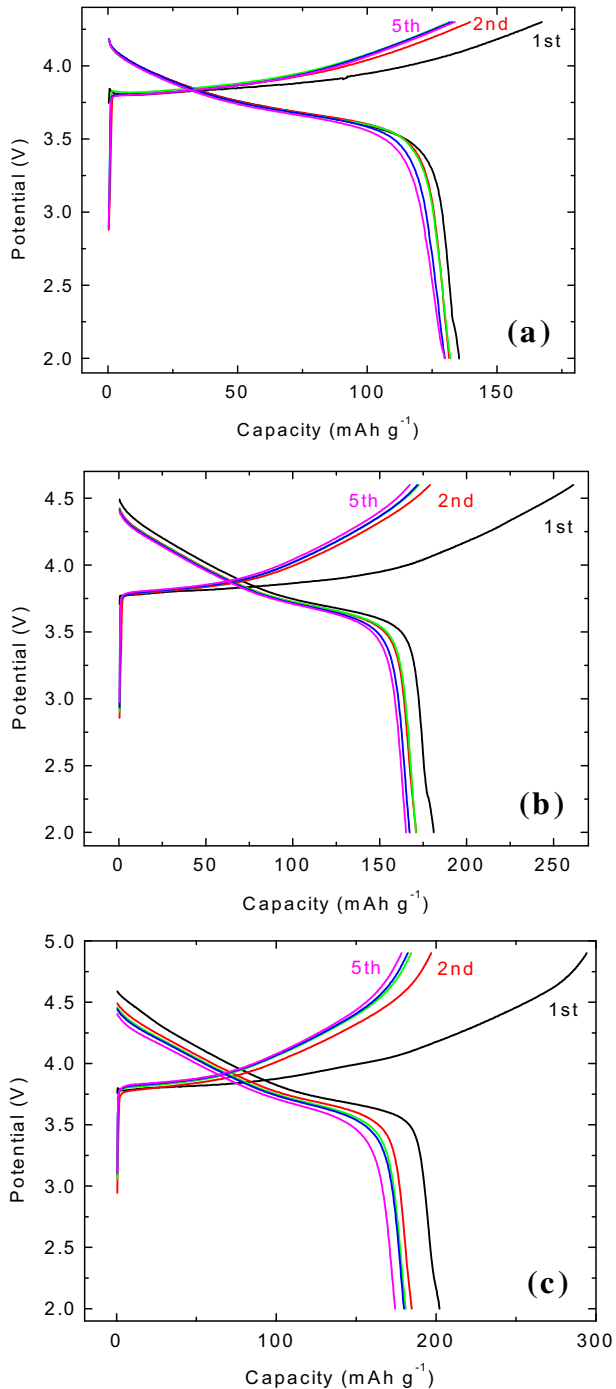


Fig. 5. Charge–discharge curves of $\text{LiNi}_{0.5}\text{Co}_{0.3}\text{Mn}_{0.2}\text{O}_2$ in different potential ranges. (a) 2.0–4.3 V; (b) 2.0–4.6 V; (c) 2.0–4.9 V.

4.6 V and 2.0–4.9 V, respectively (Here, the oxidation irreversible decomposition of electrolyte and partial reduction of SEI film should be also considered into the obtained reversible lithium storage capacities in high potential region). It suggests that excess lithium extraction results in the partially irreversible structure change and capacity fade in a broad potential range. Therefore, it is necessary to study the structural evolutions of spherical $\text{LiNi}_{0.5}\text{Co}_{0.3}\text{Mn}_{0.2}\text{O}_2$ in different working windows to find the sources of capacity loss during repeated electrochemical cycles.

Herein, *in-situ* XRD techniques are used to show the detailed structural evolutions of spherical $\text{LiNi}_{0.5}\text{Co}_{0.3}\text{Mn}_{0.2}\text{O}_2$. In the

experiment, homemade *in-situ* XRD cell is built as described by our previous papers [26,27]. The electrode for *in-situ* XRD observation is free of Al current collector with the composition of 80% active material, 10% binder and 10% conductive additive. The *in-situ* XRD cell is charged at a constant current density of 10 mA g^{-1} to reach the 4.3 V cutoff limitation with a specific charge capacity of 167.4 mAh g^{-1} , corresponding to 0.606 Li per formula released from the charge process. In the reverse lithiation process, a specific discharge capacity of 130.1 mAh g^{-1} can be delivered with the 2.0 V cutoff limitation, corresponding to 0.471 Li per formula re-storage in the electrode. Here, the Li lithiation/delithiation values per formula should include the probable capacity from the side-reaction of electrolyte and corresponding SEI film on the electrodes. In the following discussions, all the Li lithiation/delithiation values also include the extra capacity from the side-reaction of electrolyte and corresponding SEI film on the electrodes, especially for the electrode cycled in high potential ranges ($>4.3 \text{ V}$).

Fig. 7 shows the *in-situ* XRD patterns of spherical $\text{LiNi}_{0.5}\text{Co}_{0.3}\text{Mn}_{0.2}\text{O}_2$ between 2.0 and 4.3 V. The first black bold *in-situ* XRD pattern is taken at open-circuit potential before charge. In the following observation, black and red curves represent the corresponding electrochemical delithiation and lithiation processes during the initial charge–discharge cycle. The red bold and blue bold *in-situ* XRD patterns are performed at the beginning and at the end of charge process, respectively. All the diffraction peaks in the *in-situ* XRD patterns show the characteristic reflections of the rhombohedral phase and are indexed similar to the original sample. The evolutions of (003), (101), (006), (102), (104), (107), (108), (110) and (113) diffraction peaks are observed during the electrochemical charge–discharge cycle. Viewed from Fig. 7, it can be found that all the Bragg positions and intensities of characteristic peaks show slight shift upon lithium ion insertion and move back upon lithium ion extraction in 2.0–4.3 V. The strong diffraction peaks of metal Be in the *in-situ* XRD patterns are attributed to the use of metal Be window for X-ray transmission.

Fig. 8 shows the *in-situ* XRD patterns in selected 2θ regions to display the detailed evolutions of Bragg positions and diffraction intensities for $\text{LiNi}_{0.5}\text{Co}_{0.3}\text{Mn}_{0.2}\text{O}_2$ samples in a traditional cycling potential range from 2.0 to 4.3 V. Compared with the powder XRD pattern, the intensities of specific diffraction peaks are reduced by the Be window and electrolyte used in the *in-situ* XRD cell. There are 40 patterns for the *in-situ* XRD observation between 2.0 and 4.3 V, including 22 patterns taken in the charge process and 18 patterns obtained in the discharge process. In the experiment, the *in-situ* XRD pattern taken at open-circuit potential is identified as hexagonal phase H1. By tracking the evolutions of (003), (101), (006), (102) and (104) peaks as shown in Fig. 8a–i, it is obvious that the (003) peak shifts to lower 2θ angle, the (101), (102) and (104) peaks shift to higher 2θ angles, and the (006) peak disappears during the first charge process. All the diffraction peaks move back but can not return to the original positions during the reverse discharge process. The intensities of (003) and (101) peaks decrease initially in the charge process, increase to a maximum value at the end of charge and then decrease again in the discharge process. For comparison, the (104) peak decreases along with the delithiation process, reaches a minimum value at the end of charge and then increases in the delithiation process. However, the intensities and shapes of all the Bragg peaks can not restore completely after the charge–discharge cycle. All these evidences indicate that the crystal structure of $\text{LiNi}_{0.5}\text{Co}_{0.3}\text{Mn}_{0.2}\text{O}_2$ can not totally recover even though the sample is cycled in a narrow cycling potential range from 2.0 to 4.3 V.

By tracking the evolutions of (003), (101), and (104) peaks, the conversion of hexagonal phase H1 to hexagonal phase H2 can be observed upon the delithiation process and corresponding lattice

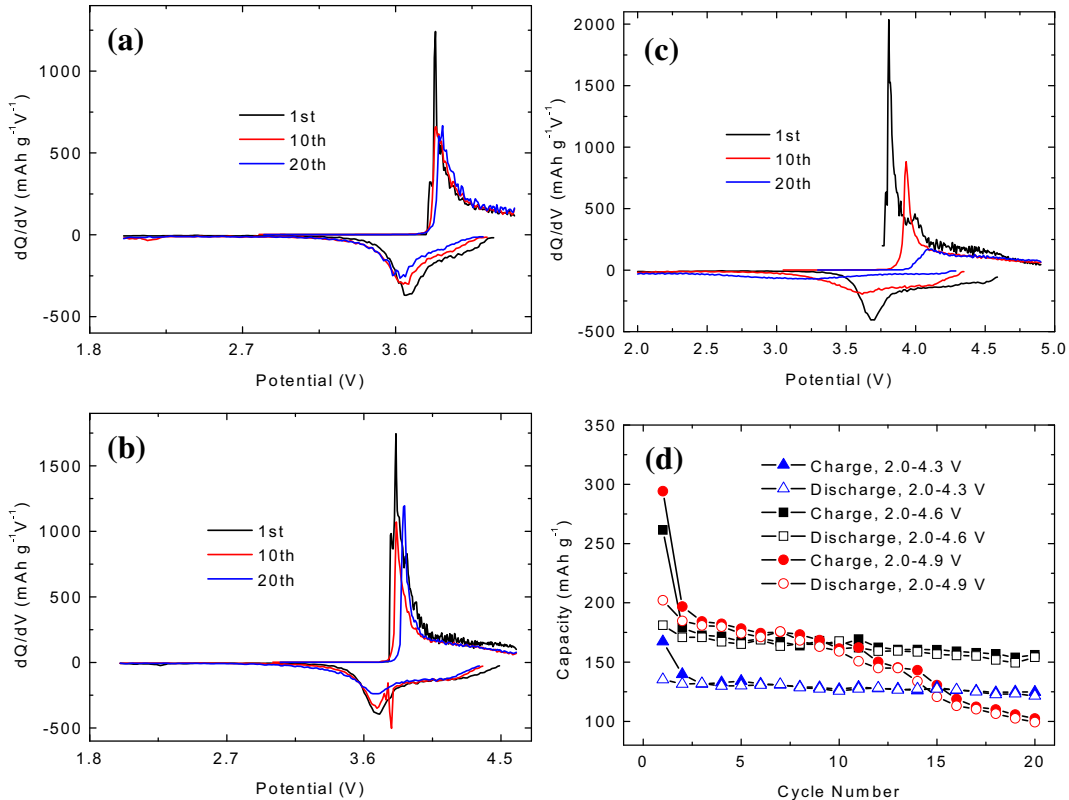


Fig. 6. Electrochemical behaviors of $\text{LiNi}_{0.5}\text{Co}_{0.3}\text{Mn}_{0.2}\text{O}_2$ in different potential ranges. (a) dQ/dV curves in 2.0–4.3 V; (b) dQ/dV curves in 2.0–4.6 V; (c) dQ/dV curves in 2.0–4.9 V; (d) cycling properties.

parameters are calculated. Both the hexagonal phase H1 and hexagonal phase H2 show the same hexagonal structure. Similar structure evolutions can be found in the layered O_3 type compounds, especially for layered LiNiO_2 systems [28–32]. As shown in Fig. 9, the lattice parameter a gradually decreases from 2.8933 to 2.8681 \AA , and lattice parameter c gradually increases from 14.2966 to 14.4152 \AA along with the charge process. The decrease of lattice parameter a is contributed to the decrease of average metal–metal distance due to the oxidation formation of transition metal ions with smaller ionic radii (Ni^{2+} : 0.69 \AA , Ni^{3+} : 0.56 \AA , Ni^{4+} : 0.48 \AA , Co^{3+} : 0.61 \AA , Co^{4+} : 0.53 \AA), which leads to a decrease of metal–oxygen distance and an increase in covalency between M–O bonds.

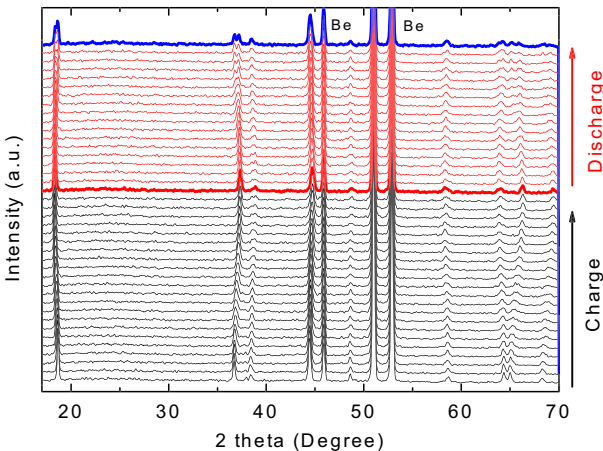


Fig. 7. *In-situ* XRD patterns of $\text{LiNi}_{0.5}\text{Co}_{0.3}\text{Mn}_{0.2}\text{O}_2$ between 2.0 and 4.3 V.

The increase of lattice parameter c is attributed to an increase of the electrostatic repulsion between the oxygen–oxygen layers due to the removal of lithium ions, which causes the shifting the (003) peak position to lower angle during a charge process to 4.3 V. As a result, the lattice volume V shows a gradual decrease from 103.6421 to 102.6898 \AA^3 along with the charge process. Furthermore, the c/a value exhibits an increase from 4.9413 to 5.0261 upon the delithiation process, which suggests that the delithiated samples possess higher hexagonal layered properties. This phenomenon is also confirmed by the evolution of (018)/(110) reflection pairs as shown in Fig. 8i. In the XRD patterns of hexagonal layered materials, the splitting of (018)/(110) Bragg peaks is always regarded as the indicator of the order characteristics of layered structure. Upon delithiation, the splitting between the (018) and (110) peaks becomes clear, suggesting that the removal of lithium ion from $\text{LiNi}_{0.5}\text{Co}_{0.3}\text{Mn}_{0.2}\text{O}_2$ increases the layered properties of the material. Upon the lithiation process, reverse but irreversible variations in the lattice parameters a , c , c/a and lattice volume V can be seen. Compared with the fresh sample before charge–discharge cycle, the lattice parameters a , c , c/a and lattice volume V of the recharged sample are 2.8878 \AA , 14.3154 \AA , 4.9573 and 103.3834 \AA^3 , respectively. In the subsequent cycles, the active material shows high-degree reversibility upon lithium ion insertion and extraction as proved by cycling properties in Fig. 6d. Therefore, the host spherical $\text{LiNi}_{0.5}\text{Co}_{0.3}\text{Mn}_{0.2}\text{O}_2$ material is favorable to be as long-term cathode material for lithium-ion batteries in the working potential range between 2.0 and 4.3 V.

In the experiment, another *in-situ* XRD cell is assembled for the *in-situ* XRD observation in a broad electrochemical window from 2.0 to 4.9 V. The *in-situ* XRD cell is charged at a constant current density of 10 mA g^{-1} to reach the 4.9 V cutoff limitation with a specific charge capacity of 270.6 mAh g^{-1} , corresponding to 0.979 Li

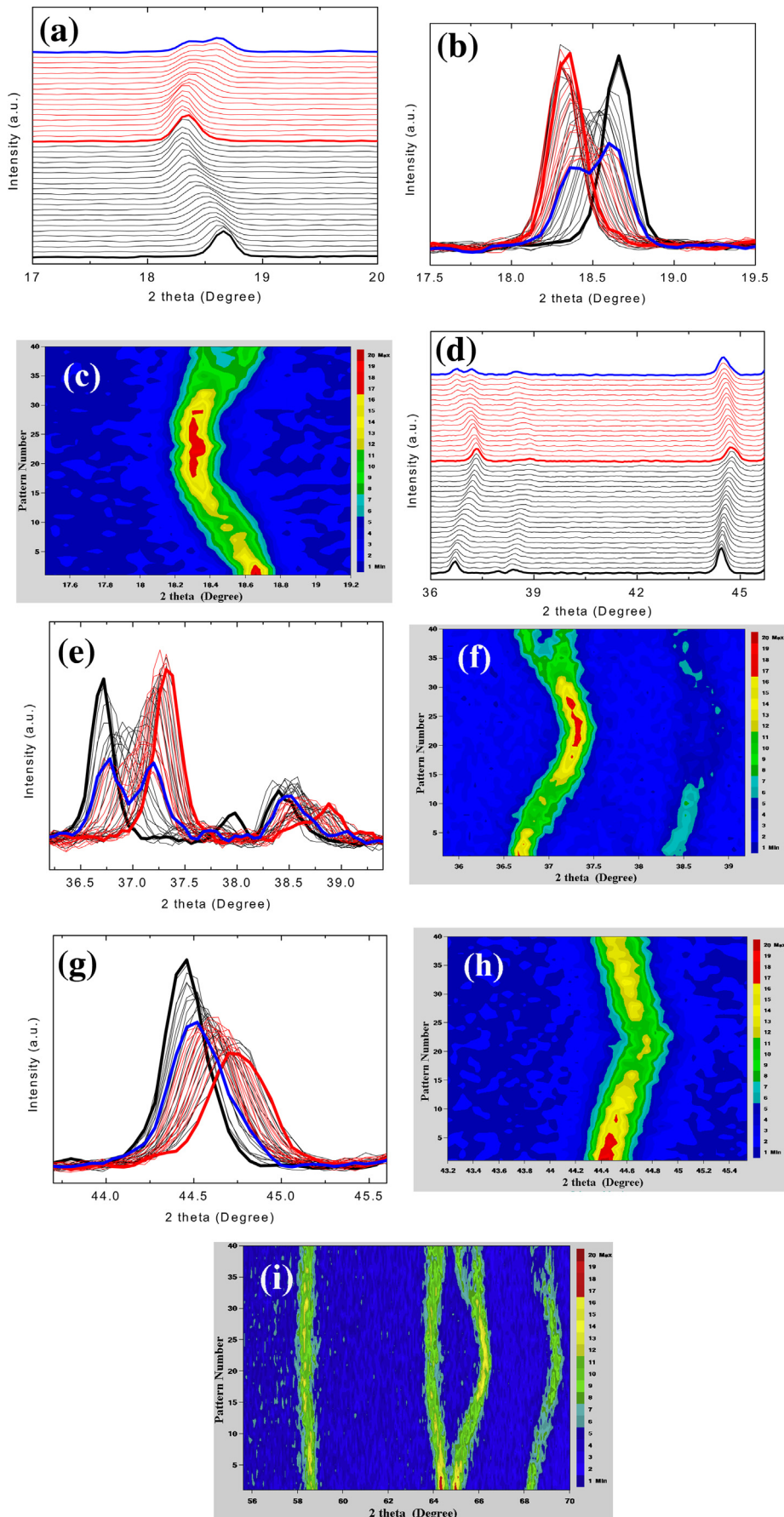


Fig. 8. Selected *in-situ* XRD patterns of $\text{LiNi}_{0.5}\text{Co}_{0.3}\text{Mn}_{0.2}\text{O}_2$ between 2.0 and 4.3 V.

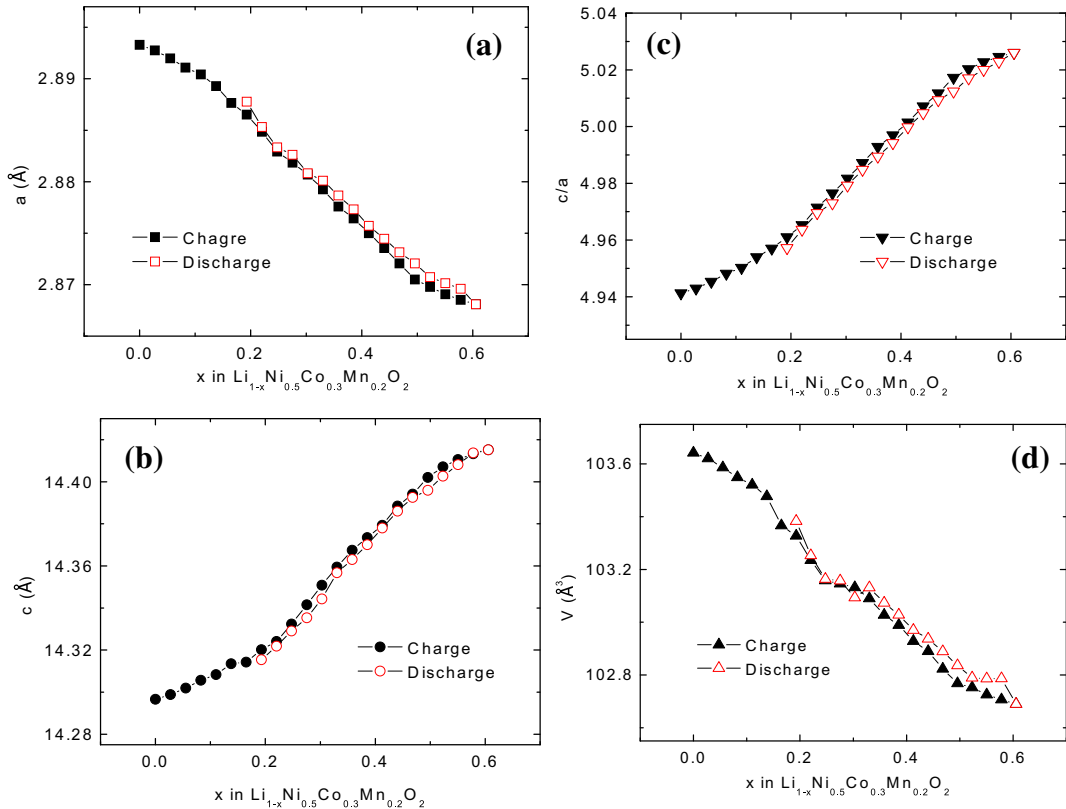


Fig. 9. The evolutions of lattice parameters (a , c and V) for $\text{LiNi}_{0.5}\text{Co}_{0.3}\text{Mn}_{0.2}\text{O}_2$ between 2.0 and 4.3 V.

per formula released from the charge process. In the reverse discharge process, a specific discharge capacity of 171.0 mAh g^{-1} can be obtained with the 2.0 V cutoff limitation, corresponding to 0.619 Li per formula re-storage in the electrode. As shown in Fig. 10, there are 39 patterns for the *in-situ* XRD observation between 2.0 and 4.9 V, including 23 patterns taken in the charge process and 16 patterns obtained in the discharge process.

With an upper cutoff limitation at 4.9 V, it can be found that the evolution of *in-situ* XRD patterns between 2.0 and 4.3 V is the same as the data shown in Fig. 8. Different structure evolution of $\text{LiNi}_{0.5}\text{Co}_{0.3}\text{Mn}_{0.2}\text{O}_2$ can be observed in the high potential region above 4.3 V. By tracking the position evolutions of (003), (101), (006), (102)

and (104) peaks as shown in Fig. 11a–i, it is clear that all the diffraction peaks show different shifting routes with those obtained in 2.0–4.3 V. The (003) peak initially shifts to lower 2θ angle and then move toward higher 2θ region in the charge process and this peak shows a reverse behavior in the discharge process. The (101), (102) and (104) peaks shift to higher 2θ angles in the charge process, and then the (101), (102) peaks retain the Bragg positions in the discharge process but (104) peak shifts back to lower 2θ angle in the charge process. The (006) peak disappears in the first charge process and does not recover in the reverse discharge process. It can also be found that all the Bragg positions move back but can not return to the original angles during the reverse discharge process.

By tracking the intensity evolutions of (003), (101) and (104) peaks as shown in Fig. 11a–i. It is obvious that the intensity of (003) peak initially decreases from pattern 1 to pattern 11, and gradually increases from pattern 11 to pattern 17 and then decrease again in the highly discharge process. In contrast, the intensity of (003) peak only shows a slight increase along with the Bragg position shifting to higher 2θ angle. The (101) and (104) peaks exhibit similar behaviors with those observed in 2.0–4.3 V. The (101) peak initially decreases in the charge process, and increases to a maximum value at the end of charge and then decreases again in the discharge process. The (104) peak gradually decreases along with the delithiation process, reaches a minimum value at the end of charge and then gradually increases in the discharge process. Compared with the results obtained in 2.0–4.3 V, it can be clearly found that the Bragg positions, relative intensities and shapes of all the diffraction peaks of recharged samples deviate more seriously from the original pattern after a full charge–discharge cycle. It indicates that the irreversibility of structural changes in a higher working potential region between 2.0 and 4.9 V is more serious than that in a traditional working potential region between 2.0 and 4.3 V.

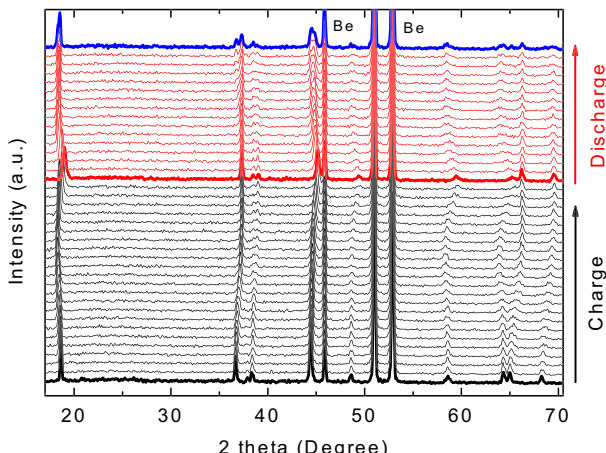


Fig. 10. *In-situ* XRD patterns of $\text{LiNi}_{0.5}\text{Co}_{0.3}\text{Mn}_{0.2}\text{O}_2$ in a high potential region between 2.0 and 4.9 V.

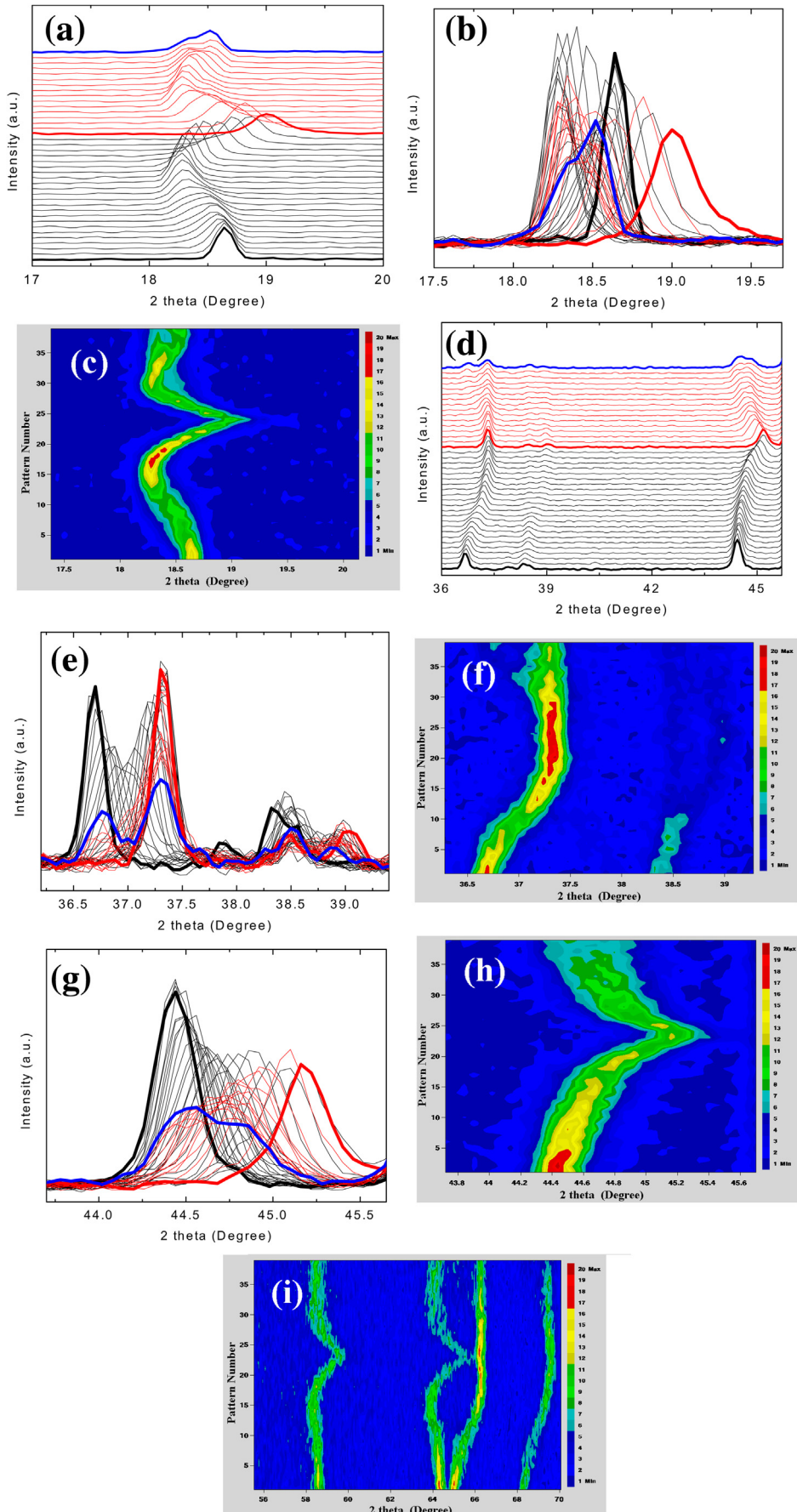


Fig. 11. Selected *in-situ* XRD patterns of $\text{LiNi}_{0.5}\text{Co}_{0.3}\text{Mn}_{0.2}\text{O}_2$ in a high potential region between 2.0 and 4.9 V.

By tracking the variations of lattice parameters, the conversion of hexagonal phase H1 to hexagonal phase H2 and hexagonal phase H3 can be observed upon the deep-degree delithiation and lithiation processes. All the three hexagonal phases H1, H2 and H3 show the same hexagonal structure. Similar variations can be observed in layered LiNiO_2 systems or other layered O_3 type compounds cycled in high potential regions [28–30]. The evolutions of lattice parameters a , c , c/a and lattice volume V between 2.0 and 4.9 V are shown in Fig. 12, which are similar with the structural evolutions of $\text{LiNi}_{0.5}\text{Mn}_{0.5}\text{O}_2$ or $\text{LiNi}_{0.5}\text{Mn}_{0.45}\text{Ti}_{0.05}\text{O}_2$ with a delithiation of about 0.80 Li per formula [33]. It is clear that the lattice parameter a shows a rapid decrease from 2.8933 to 2.8637 \AA with 0.681 Li per formula extraction from the structure and reduces slowly to a minimum value of 2.8593 \AA with a delithiation of 0.979 Li per formula. Upon lithiation, the lattice parameter a shows a gradual increase to 2.8778 \AA , which is smaller than that of the pristine sample. The difference (Δa) in lattice parameter a before and after cycle in 2.0–4.9 V is 0.0155 \AA , which is larger than that ($\Delta a = 0.0055 \text{\AA}$) obtained in 2.0–4.3 V. For comparison, lattice parameter c gradually increases at the begin of charge, reaches a maximum value of 14.4152 \AA with a delithiation of 0.681 Li per formula, and then gradually decreases to a minimum value of 14.3206 \AA after full delithiation. This phenomenon is in good accordance with the change in Bragg position of the (003) reflection. The appearance of turning point in Fig. 12b suggests the formation of hexagonal phase H3, which is also confirmed by the indexing of XRD pattern. The decrease of lattice parameter c in highly delithiated states (>0.681 Li) is probably attributed to the decrease of electrostatic repulsion between the oxygen–oxygen layers, which is resulted from the increase of covalency between M–O bonds after the deep-degree removal of lithium ions. During

the discharge process, lattice parameter c increases gradually and reaches a maximum value of 14.4134 \AA with a lithiation of 0.298 Li per formula, and then gradually decreases again but can not reach the original value before charge–discharge cycle. The difference (Δc) in lattice parameter c before and after cycle in 2.0–4.9 V is 0.0624 \AA , which is larger than that ($\Delta c = 0.0188 \text{\AA}$) obtained in 2.0–4.3 V. Furthermore, the evolution of c/a values follows with the shifting trend of lattice parameter c , exhibits an increase from 4.9413 to 5.0339 and then decreases to a final value of 5.0085 along with the delithiation process, which indicates that the hexagonal phase H2 shows a highly hexagonal layered property and hexagonal phase H3 reveals rather low hexagonal layered property. This result is also in agreement with the evolution of (018)/(110) diffraction pairs as shown in Fig. 11i, which displays a splitting behavior at the beginning of charge and then almost merges into one peak upon a deep-degree delithiation to 4.9 V.

Based on the continuous change of lattice parameters a and c , the lattice volume V also shows a larger difference of 0.6579 \AA^3 before and after cycle in 2.0–4.9 V than the value ($\Delta V = 0.2587 \text{\AA}^3$) observed in 2.0–4.3 V. It tells that the volume expansion of active grains is more serious with a higher cutoff limitation at 4.9 V, which results in the poor electrochemical properties as shown in Fig. 6d. Fig. 13 shows the structural evolutions of $\text{LiNi}_{0.5}\text{Co}_{0.3}\text{Mn}_{0.2}\text{O}_2$ at 11th cycle and 20th cycle. It proves that the disappearance of hexagonal phase H3 and the structure of rhombohedral layered $\text{LiNi}_{0.5}\text{Co}_{0.3}\text{Mn}_{0.2}\text{O}_2$ is partially destroyed upon repeated cycles. Besides, the surface of Be window in the *in-situ* cell for X-ray transmission was also oxidized into BeO after long-term electrochemical cycles in 2.0–4.9 V. According to the turning points from hexagonal phase H2 to hexagonal phase H3 shown in Fig. 12b and c and the excellent cycling properties of $\text{LiNi}_{0.5}\text{Co}_{0.3}\text{Mn}_{0.2}\text{O}_2$ in 2.0–

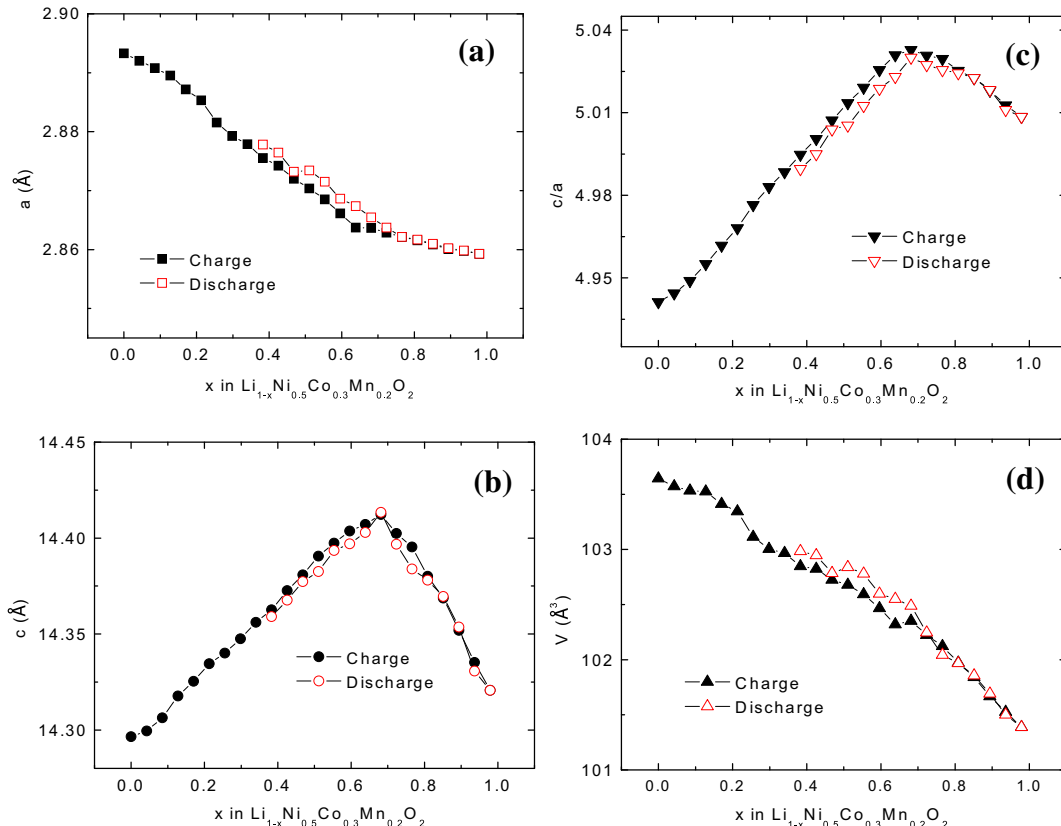


Fig. 12. The evolutions of lattice parameters (a , c and V) for $\text{LiNi}_{0.5}\text{Co}_{0.3}\text{Mn}_{0.2}\text{O}_2$ in a high potential region between 2.0 and 4.9 V.

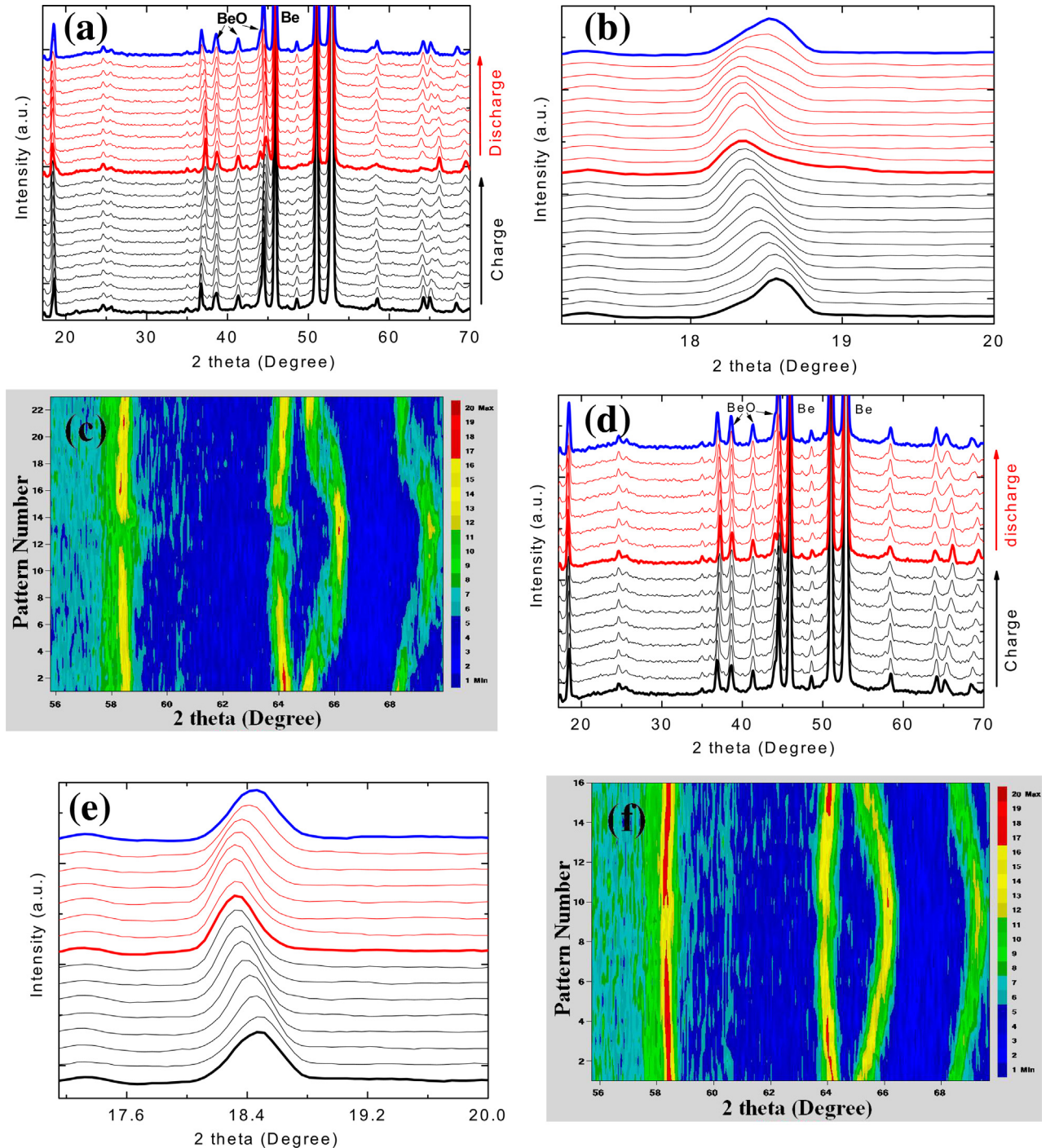


Fig. 13. *In-situ* XRD patterns of $\text{LiNi}_{0.5}\text{Co}_{0.3}\text{Mn}_{0.2}\text{O}_2$ at the 10th cycle (a–c) and 20th cycle (d–f) in a high potential region between 2.0 and 4.9 V.

4.6 V shown in Fig. 6d, it can be deduced that the formation of hexagonal H3 phase is an indicator for the appearance of poor cyclability and low reversible capacity, where the transition from hexagonal phase H2 to hexagonal phase H3 occurs at around 4.7 V. As a result, the suppression of hexagonal phase H3 for $\text{LiNi}_{0.5}\text{Co}_{0.3}\text{Mn}_{0.2}\text{O}_2$ in this study is expected to achieve a better structural stability and long-term cyclability. Herein, the favorable lithium release content for the cathode is probable to be 0.681 Li per formula or less, corresponding to a maximum specific capacity of 188.2 mAh g^{-1} . Thus, spherical $\text{LiNi}_{0.5}\text{Co}_{0.3}\text{Mn}_{0.2}\text{O}_2$ cathode shows an outstanding cyclability with a reversible discharge capacity of 154.2 mAh g^{-1} in 2.0–4.6 V after 20 cycles.

4. Conclusions

A kind of Ni–Co–Mn ternary transition metal cathode materials, $\text{LiNi}_{0.5}\text{Co}_{0.3}\text{Mn}_{0.2}\text{O}_2$, is synthesized by firing the mixture of $\text{Ni}_{0.5}\text{C}_{0.3}\text{Mn}_{0.2}[\text{OH}]_2$ and $\text{LiOH}\cdot\text{H}_2\text{O}$. The precursor $\text{Ni}_{0.5}\text{Co}_{0.3}\text{Mn}_{0.2}[\text{OH}]_2$ hydroxides are coprecipitated by adding the LiOH solution into an aqueous mixed solution containing Co^{2+} , Ni^{2+} , and Mn^{2+} with the molar ratio of Ni:Co:Mn = 5:3:2. Powder XRD pattern of the fresh sample shows that there is the existence of doublets at (006)/(102) and (108)/(110) reflections in the diffraction pattern, indicating the well-defined layered structure of as-prepared product with $c/a = 4.9413$. Electrochemical and *in-situ* XRD evidences show that

spherical $\text{LiNi}_{0.5}\text{Co}_{0.3}\text{Mn}_{0.2}\text{O}_2$ cathode cycled in higher potential region exhibits poorer electrochemical properties, which is attributed to the formation of hexagonal phase H3 and electrolyte irreversible decomposition in high potential regions. Furthermore, *in-situ* XRD patterns also show that the formation of hexagonal phase H3 at around 4.7 V in the charge process is the main structure destroyer resulting in poor cyclability and low reversible capacity. Therefore, spherical $\text{LiNi}_{0.5}\text{Co}_{0.3}\text{Mn}_{0.2}\text{O}_2$ displays a high reversible lithium storage capacity of 154.2 mAh g⁻¹ in 2.0–4.6 V by suppressing the formation of hexagonal phase H3.

Acknowledgment

This work is sponsored by National 863 Program (2013AA050901), National Natural Science Foundation of China (No. 51104092) and Qianjiang Talent Project of Zhejiang Province (2011R10089). The work is also supported by K. C. Wong Magna Fund in Ningbo University, Open Foundation of State Key Laboratory of Materials Processing and Die & Mould Technology (2012-P01), Open Foundation of State Key Laboratory of Electronic Thin Films and Integrated Devices (KJFJ201209) and Open Foundation of State Key Laboratory Breeding Base of Green Chemistry-Synthesis Technology (GCKF2012002).

References

- [1] T. Ohzuku, Y. Makimura, *Chem. Lett.* 7 (2001) 642.
- [2] N.N. Sinha, N. Munichandraiah, *J. Electrochem. Soc.* 157 (2010) A647.
- [3] S. Komaba, K. Yoshii, A. Ogata, I. Nakai, *Electrochim. Acta* 54 (2009) 2353.
- [4] S.W. Woo, S.T. Myung, H. Bang, D.W. Kim, Y.K. Sun, *Electrochim. Acta* 54 (2009) 3851.
- [5] J. Jiang, T. Buhrmester, K.W. Eberman, L.J. Krause, J.R. Dahn, *J. Electrochem. Soc.* 152 (2005) A19.
- [6] D.L. Zeng, J. Cabana, W.S. Yoon, C.P. Grey, *Chem. Mater.* 22 (2010) 1209.
- [7] M. Noh, J. Cho, *J. Electrochem. Soc.* 160 (2013) A105.
- [8] J.Z. Kong, F. Zhou, C.B. Wang, X.Y. Yang, H.F. Zhai, H. Li, J.X. Li, Z. Tang, S.Q. Zhang, *J. Alloys Compd.* 554 (2013) 221.
- [9] J. Li, J.M. Zheng, Y. Yang, *J. Electrochem. Soc.* 154 (2007) A427.
- [10] X.H. Xiong, Z.X. Wang, H.J. Guo, Q. Zhang, X.H. Li, *J. Mater. Chem. A* 1 (2013) 1284.
- [11] S.U. Woo, B.C. Park, C.S. Yoon, S.T. Myung, J. Prakash, Y.K. Sun, *J. Electrochem. Soc.* 154 (2007) A649.
- [12] Y.K. Sun, S.T. Myung, B.C. Park, J. Prakash, I. Belharouak, K. Amine, *Nat. Mater.* 8 (2009) 320.
- [13] L.P. Zhang, T. Dong, X.J. Yu, Y.H. Dong, Z.D. Zhao, H. Li, *Mater. Res. Bull.* 47 (2012) 3269.
- [14] H. Gao, Y. Zhang, J. Zhang, B.J. Xia, *Solid State Ion.* 176 (2005) 1207.
- [15] Y.S. Lee, D. Ahn, Y.H. Cho, T.E. Hong, J. Cho, *J. Electrochem. Soc.* 158 (2011) A1354.
- [16] X.X. Zuo, C.J. Fan, J.S. Liu, X. Xiao, J.H. Wu, J.M. Nan, *J. Power Sources* 229 (2013) 308.
- [17] J.W. Lee, J.H. Lee, T.T. Viet, J.Y. Lee, J.S. Kim, C.H. Lee, *Electrochim. Acta* 55 (2010) 3015.
- [18] Y. Chen, G.F. Xu, J.L. Li, Y.K. Zhang, Z. Chen, F.Y. Kang, *Electrochim. Acta* 87 (2013) 686.
- [19] J.F. Ni, H.H. Zhou, J.T. Chen, X.X. Zhang, *Electrochim. Acta* 53 (2008) 3075.
- [20] R. Chitrakar, S. Kasaishi, A. Umeno, K. Sakane, N. Takagi, Y.S. Kim, K. Ooi, *J. Solid State Chem.* 169 (2002) 35.
- [21] W.W. Huang, R. Frech, *Solid State Ion.* 86–88 (1996) 395.
- [22] M. Kerlau, M. Marcinek, V. Srinivasan, R.M. Kostecki, *Electrochim. Acta* 52 (2007) 5422.
- [23] C.S. Johnson, N.C. Li, C. Lefief, J.T. Vaughey, M.M. Thackeray, *Chem. Mater.* 20 (2008) 6095.
- [24] H.H. Hayley, N. Yabuuchi, Y.S. Meng, S. Kumar, J. Breger, C.P. Grey, S.H. Yang, *Chem. Mater.* 19 (2007) 2551.
- [25] J. Breger, Y.S. Meng, Y. Hinuma, S. Kumar, K. Kang, S.H. Yang, G. Ceder, C.P. Grey, *Chem. Mater.* 18 (2006) 4768.
- [26] J. Shu, M. Shui, D. Xu, Y.L. Ren, D.J. Wang, Q.C. Wang, R. Ma, W.D. Zheng, S. Gao, L. Hou, J.J. Xu, J. Cui, Z.H. Zhu, M. Li, *J. Mater. Chem.* 22 (2012) 3035.
- [27] J. Shu, M. Shui, D. Xu, S. Gao, T.F. Yi, D.J. Wang, X. Li, Y.L. Ren, *Ionics* 17 (2011) 503.
- [28] X.Q. Yang, J. McBreen, W.S. Yoon, C.P. Grey, *Electrochim. Commun.* 4 (2002) 649.
- [29] P.Y. Liao, J.G. Duh, H.S. Sheu, *J. Power Sources* 183 (2008) 766.
- [30] D. Mohanty, S. Kalnaus, R.A. Meissner, K.J. Rhodes, J.L. Li, E.A. Payzant, D.L. Wood III, C. Daniel, *J. Power Sources* 229 (2013) 239.
- [31] C.R. Fell, M. Chi, Y.S. Meng, J.L. Jones, *Solid State Ion.* 207 (2011) 44.
- [32] W. Sub Yoon, N.J. Kim, X.Q. Yang, J. McBreen, C.P. Grey, *J. Power Sources* 119–221 (2003) 649.
- [33] S.T. Myung, S. Komaba, K. Hosoya, N. Hirosaki, Y. Miura, N. Kumagai, *Chem. Mater.* 17 (2005) 2427.